GEOPHYSICAL RESEARCH LETTERS, VOL. 34, L01605, doi:10.1029/2006GL028170, 2007

Hotspots of deep ocean mixing on the Oregon continental slope

J. D. Nash,[1] M. H. Alford,[2] E. Kunze,[3] K. Martini,[2] and S. Kelly[1]

Received 13 September 2006; revised 9 November 2006; accepted 1 December 2006; published 9 January 2007.

[1] Two deep ocean hotspots of turbulent mixing were found over the Oregon continental slope. Thorpe-scale analyses indicate time-averaged turbulent energy dissipation rates of $\epsilon > 10^{-7}$ W/kg and eddy diffusivities of $K_\rho \sim 10^{-2}$ m^2/s at both hotspots. However, the structure of turbulence and its generation mechanism at each site appear to be different. At the 2200-m isobath, sustained >100-m high turbulent overturns occur in stratified fluid several hundred meters above the bottom. Turbulence shows a clear 12.4-h periodicity proposed to be driven by flow over a nearby 100-m tall ridge. At the 1300-m isobath, tidally-modulated turbulence of similar intensity is confined within a stratified bottom boundary layer. Along-slope topographic roughness at scales not resolved in global bathymetric data sets appears to be responsible for the bulk of the turbulence observed. Such topography is common to most continental slopes, providing a mechanism for turbulence generation in regions where barotropic tidal currents are nominally along-isobath. **Citation:** Nash, J. D., M. H. Alford, E. Kunze, K. Martini, and S. Kelly (2007), Hotspots of deep ocean mixing on the Oregon continental slope, *Geophys. Res. Lett.*, *34*, L01605, doi:10.1029/2006GL028170.

1. Introduction

[2] Most continental slopes are inefficient generators of low-mode internal tides because barotropic tidal flows are generally parallel to large-scale isobaths. Yet many continental slopes have significant small-scale topographic roughness with $\lambda_h < 10$ km both along and across the nominal slope. High-wavenumber internal waves generated by flow over this small-scale topography [*Kunze and Llewellyn Smith*, 2004; *Goff and Jordan*, 1988] are believed to play the largest role in local mixing [*St. Laurent and Nash*, 2004; *Garrett and Kunze*, 2007]. Tidal mixing can thus result from local generation by tidal flow over small-scale topography [*Thorpe*, 1992; *Legg*, 2004] or from the shoaling of remotely-generated internal tides [*Nash et al.*, 2004].

[3] The ability of continental slopes to dissipate significant barotropic and baroclinic tidal energy may elevate their importance in the ocean energy budget. Supporting this view, [*Moum et al.*, 2002] found strong turbulence over the Oregon continental slope of similar intensity to that over other deep sites of rough topography such as the Mid-Atlantic Ridge [*Ledwell et al.*, 2000]. They hypothesized that the mixing over the Oregon slope was driven by an intensified semidiurnal wavefield associated with an abundance of near-critical bathymetry.

[4] To determine whether remote or local processes lead to the turbulent energy dissipation ϵ found over the Oregon slope, we conducted a 40-day field program to observe the internal wave climate and mixing. Over all deep sites sampled, turbulence within 500 mab (meters above the bottom) was strong and of the same order of magnitude as found by [*Moum et al.*, 2002] nearby. Near the 2200-m isobath, tidally-modulated vertical overturns (statically unstable regions) exceeding 100 m were repeatedly seen as far as 400 m above the bottom, while at the 1300-m isobath, the turbulence appears connected to the bottom. At both sites, dissipation was a factor of ten stronger than that observed elsewhere on the slope, suggesting that deep mixing over the Oregon continental slope is not only elevated but also highly spatially heterogeneous.

2. Site Setting and Methods

[5] As typical of the continental slope lining the western United States, our study region (Figures 1 and 2) contains pinnacles, cliffs, valleys and canyons from former submarine landslides (100-m resolution bathymetry courtesy J. Chaytor and C. Goldfinger [*Romsos et al.*, 2006]). Low-passed (1-km cutoff) slope alternates between semidiurnal sub- and super-criticality on scales of 5–10 km (Figure 2b) where a critical slope is defined as $s/\alpha \sim 1$, $s = |\nabla H|$ is the bottom slope and $\alpha = \sqrt{(\omega^2 - f^2)/(N^2 - \omega^2)}$ the slope of an internal wave characteristic with frequency ω. RMS topographic height in the 200–1000-m waveband (H_{rms}, computed as the square root of the variance of 2D high-pass filtered bottom depth) is elevated broadly in a 20-km region between the 1200-m isobath and the abyssal seafloor, with a local maximum in a 5-km band below the 2000-m isobath (Figures 1b and 2a). Barotropic tides are predominantly semidiurnal, approximately 0.05–0.08 m/s, with principal axes aligned approximately N-S, parallel to the continental slope [*Egbert*, 1997, Figure 1].

[6] During Sept–Oct 2005, we obtained the following shipboard and moored observations (Figure 2):

[7] 1. Forty-day moored profiler timeseries of velocity and density were acquired at five locations spanning the slope with 8.5-km horizontal separation to capture slope dynamics (13 Sept.–23 Oct. 2006). An additional moored profiler (M1) was deployed 100 km offshore to capture the net incoming/outgoing internal tide over the same time period. One slope mooring (M2, at 3000-m depth) was not recovered. Over the slope, profiles were obtained every 1–2 hours from 50 m below the surface to 12–14 m above the bottom (mab); 1000 mab at offshore station M1. Profiler data at M1 was augmented by a VACM at 40 mab. At M3

[1] College of Oceanic and Atmospheric Sciences, Oregon State University, Corvallis, Oregon, USA.
[2] Applied Physics Laboratory and School of Oceanography, University of Washington, Seattle, Washington, USA.
[3] School of Earth and Ocean Science, University of Victoria, Victoria, British Columbia, Canada.

0094-8276/07/2006GL028170$05.00

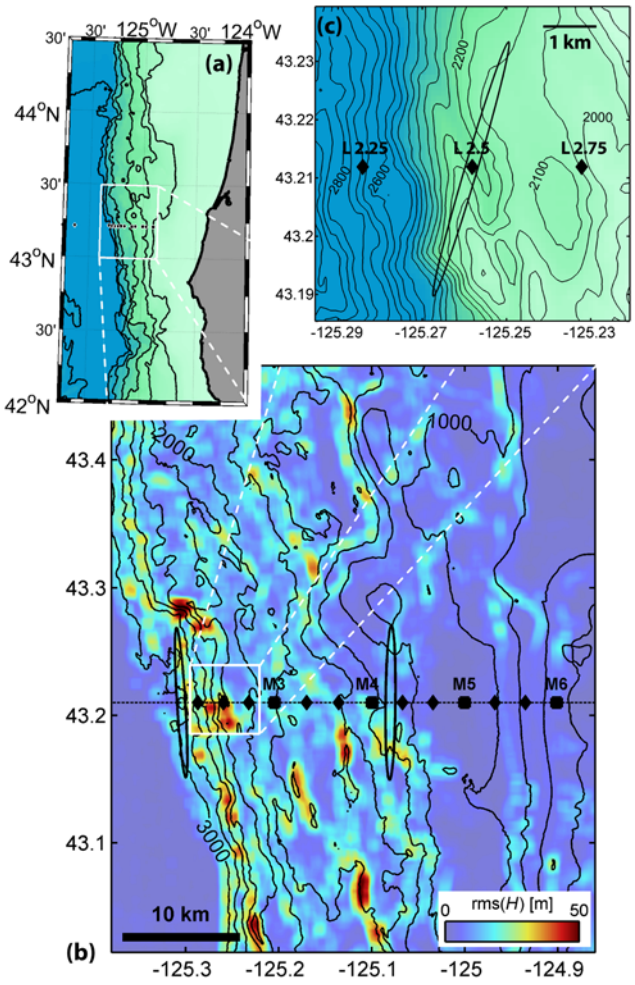

Figure 1. (a) Bathymetry (500-m contour interval) of the Oregon continental slope. (b) Roughness H_{rms} (colors), moored profiler locations (squares), CTD/LADCP and XCP stations (diamonds), TPXO.5 barotropic tidal ellipses (black [*Egbert*, 1997]) and bottom contours (200-m interval) in our study region (indicated in Figure 1a in white). (c) Bottom depth (50-m contour interval), observed near-bottom (0–500 mab) ellipse, and CTD/LADCP station locations near the 2200-m hotspot (region indicated in Figure 1b in white). 12% of the domain shown in Figure 1b has $H_{rms} > 20$ m.

and M5, upward-looking 300 kHz RDI ADCPs were deployed below the subsurface float at 60-m depth.

[8] 2. A 24-h XCP survey with 6 stations spaced <3 km apart spanning water depths of 750–1710 m. Stations were sampled every 3 h except 4.3, which was sampled every 1.5 h.

[9] 3. CTD/LADCP timeseries were acquired at eight stations spanning the slope but biased towards water depths $H > 2000$ m, i.e., below the range of XCPs. Each station was occupied for 15–48 hours. Enhanced near-bottom sampling was achieved by yo-yoing from bottom to 500 mab every 30 minutes at the deep stations. The CTD/LADCP was brought to the surface every 3 h to capture the full-depth semidiurnal signal.

[10] Turbulence was inferred using two methods. Thorpe scale analysis of density overturns from moored-profiler and shipboard CTD yields the turbulent dissipation rate $\epsilon_i = 0.64 L_{T_i}^2 N_i^3$, where N_i and L_{T_i} represent the Thorpe-resorted stratification and rms Thorpe displacement for the ith overturning region [*Dillon*, 1982]. Each L_{T_i} is rejected if smaller than the expected (spurious) values for depth and density imprecision [*Alford et al.*, 2006]. Following *Gregg* [1989] and *Gregg and Kunze* [1991], ϵ was parameterized from XCP data and found consistent with Thorpe estimates at stations where XCP and CTD measurements coincided (stations 3.3, 4.3 and 5.3). For both overturn and Gregg-Henyey ϵ, diffusivity was computed as $K_\rho = 0.2\epsilon N^{-2}$ [*Osborn*, 1980].

3. Observations

[11] High near-bottom turbulent energy dissipation rates span the 20-km region of enhanced roughness (Figure 2, 43.21° N, 125.05–125.3° W). Within 500 mab, time-average K_ρ were 10^{-4}–10^{-3} m^2/s above rough topography,

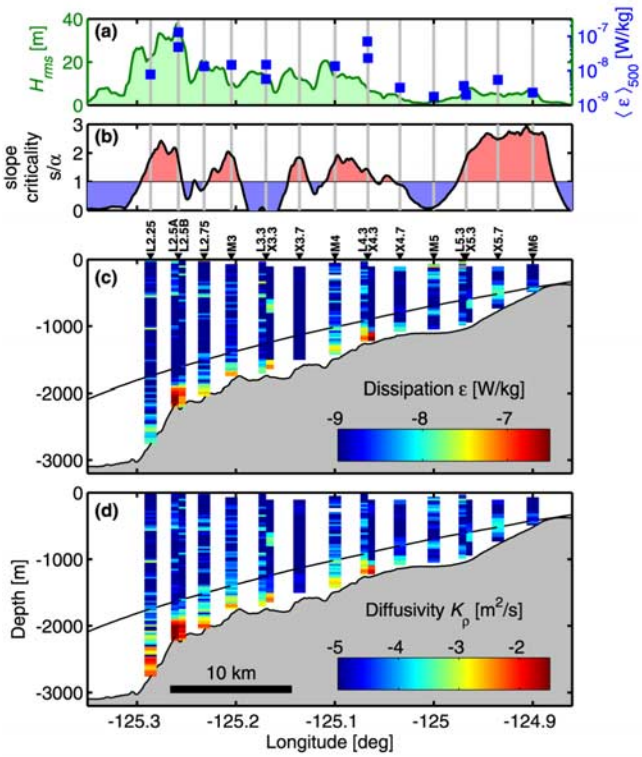

Figure 2. Cross-slope section of (a) rms topographic height in the 200–1000 m waveband (H_{rms}, green shading) (b) semidiurnal slope criticality (>1000-m scales), (c) turbulent energy dissipation rate ϵ, and (d) turbulent diffusivity K_ρ. Also shown in Figure 2a is mean ϵ within 500 mab ($\langle\epsilon\rangle_{500}$) for each station occupation. A semidiurnal characteristic is shown in Figures 2c and 2d to illustrate the slope criticality, and is not intended to represent a beam emanating from the shelf break. Station types are indicated above Figure 2c; M-, L- and X- respectively represent timeseries averages from moored profilers, CTD/LADCP and XCP. Some stations were occupied on multiple occasions and with different instrumentation as indicated. Only data near the slope are shown; an additional mooring and two CTD/LADCP stations extend to 126° 15′ W.

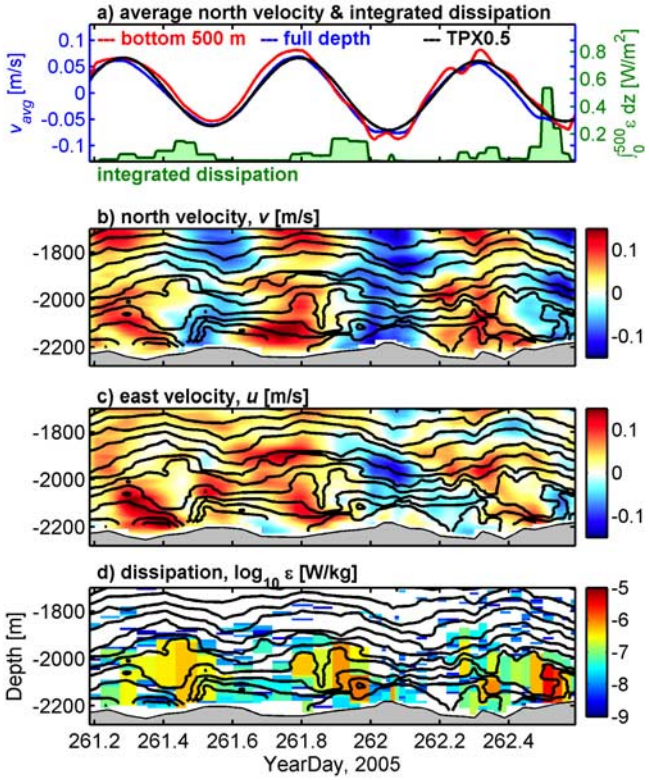

Figure 3. Timeseries at LADCP/CTD station L2.5 at the 2200-m isobath (first occupation): (a) observed (blue) and TPXO.5 (black, [*Egbert*, 1997]) barotropic N-S velocity (v), as well as 500-mab depth-mean v and depth-integrated ϵ (red, green), (b) meridional velocity v, (c) zonal velocity u and (d) inferred turbulent dissipation rate ϵ. In Figures 3b–3d, isopycnals are contoured in black.

relaxing to open-ocean values ($K_\rho \sim 10^{-5}$ m^2/s [*Gregg*, 1989]) in the upper water column and over the smoother, shallow sites east of 125.05° W. At station 2.5 (water depth 2200 m), $K_\rho > 10^{-2}$ m^2/s as far as 300 mab. Henceforth termed the "2200-m hotspot", station 2.5 is a site of both high H_{rms} (Figures 1b and 2a) and near-critical slope (Figure 2b) and was sampled for a total of 48 h on two occasions separated by 5 days. At this site, Thorpe scales exceeding 100 m ($\epsilon > 10^{-6}$ W/kg) were repeatedly observed several hundred meters off the bottom, within stratification $N \approx 2 \times 10^{-3}$ rad s^{-1}. High ϵ was also observed in the stratified bottom boundary layer at station 4.3, the "1300-m hotspot." In the following, we examine signals at the 2200-m and 1300-m hotspots.

[12] The temporal evolution of near-bottom velocity, density, and turbulent dissipation at the 2200-m hotspot is presented in Figure 3. Apart from subinertial eastward flow of ~0.04 m/s prior to yearday 262 (Figure 3c), signals are predominantly semidiurnal. Observed barotropic currents (Figure 3a, blue) are 0.07 m/s and oriented N-S, in agreement with TPXO.5 (black). Baroclinic motions with O(500 m) vertical wavelength and 0.02–0.04 m/s amplitude (Figures 3b and 3c) only weakly alter near-bottom depth averages (Figure 3a, red). However, these internal motions deflect isopycnals downward below ≈2100 m while fluid above is displaced upward. Turbulent energy dissipation (Figures 3a and 3d) is elevated below 1900 m and in phase with the resultant expansive strain (isopycnal stretching) as observed elsewhere by *Alford and Pinkel* [2000] and *Levine and Boyd* [2006].

[13] Upward isopycnal displacements above ≈1900 m (and hence expansive strain near 2100 m) lag northward velocity by approximately 90°, consistent with near-bottom northward flow up a bottom that slopes upward to the north (i.e., $\xi = \int w\, dt$, with $w = \frac{dH}{dy} v_o \cos(\omega t)$). But, in addition to the large-scale slope, a 100-m tall ridge (located to the SW and oriented NW-SE, Figure 1c) is upstream of the site during the northeastward flows occurring prior to high-dissipation events. We suspect this ridge may generate the near-bottom northeastward flow (locally downslope) that forms the lower boundary for expansive strain and high dissipation events (i.e., at yeardays 261.3, 261.8, 262.4). However, the details are unclear. Since the barotropic flow is the same magnitude as the group velocity for a 500-m vertical wavelength internal wave and $NH/u \sim$ O(1), wave generation, flow separation and 3D effects are possible [*Baines*, 1982].

[14] At the 1300-m hotspot (station 4.3), strong turbulence ($\epsilon \sim 10^{-7}$ W/kg, $K_\rho \sim 10^{-2}$ m^2/s) was observed during both XCP and CTD occupations (separated by 5 days; 35-h total sampling.) This site is located on the eastern edge of the region of enhanced H_{rms} (Figure 2a, green), with nominally critical slope. While turbulence at this station also exhibits ~12-h periodicity, it contrasts with the 2200-m hotspot in that $K_\rho \sim 10^{-2}$ m^2/s was confined within 150 mab and most intense at the bottom. Furthermore, the vertical structure of both velocity and vertical displacement shows significant vertical phase propagation. Interpretation of the dynamics at the 1300-m hotspot is the subject of ongoing investigation. At the remaining sites, the phasing between tidal velocity, strain and dissipation is less clear.

[15] A summary of ϵ and K_ρ for all stations is shown in Figure 4. Based on our limited sampling (Figure 4a), bottom roughness H_{rms} appears to contribute to near-bottom $\langle\epsilon\rangle_{500}$ (mean ϵ within 500 mab), as suggested by *Polzin* [2004]. Other factors must also be important, since H_{rms} does not explain the high $\langle\epsilon\rangle_{500}$ at station 4.3 (green). We postulate internal tide interactions with near-critical topography. It is noteworthy that weak dissipation occurs at shallow sites (see Figure 2) in spite of the classical scaling $\epsilon \propto N^2$ [*Gregg*, 1989], which would suggest the opposite relation.

[16] Mean vertical profiles of inferred turbulent dissipation rate and eddy diffusivity are shown in Figures 4b and 4c. Near-bottom ϵ and K_ρ are more than a factor of ten greater at the 2200-m (red) and 1300-m (green) hotspots than at the other stations (blue). Excluding the hotspots, the magnitude and vertical decay scale of ϵ and K_ρ profiles are similar to those observed over rough topography elsewhere [*Ledwell et al.*, 2000; *Moum et al.*, 2002; *Nash et al.*, 2004; *Klymak et al.*, 2006] (compare blue and dashed lines). Averages of dissipation and inferred diffusivity that include the hotspots (gray line) are an order of magnitude higher within 400 mab.

4. Energetics

[17] Even excluding the hotspots, the mean dissipation rate in the bottom 500 m is $\langle\epsilon\rangle_{500}^{non\text{-}hotspots} = 0.65 \times$

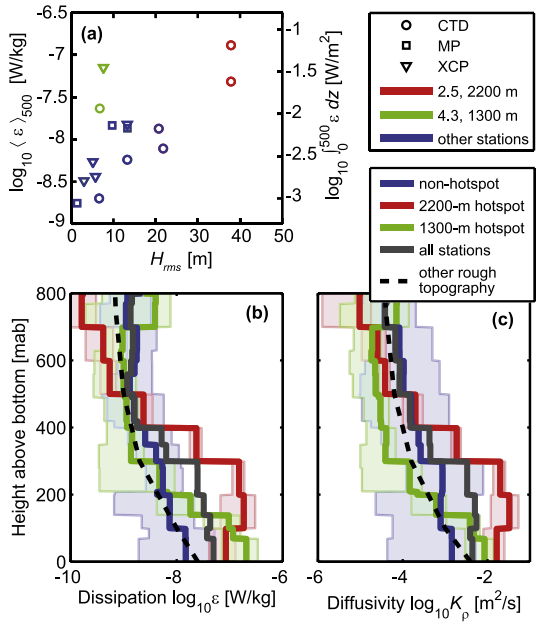

Figure 4. (a) Near bottom dissipation $\langle\epsilon\rangle_{500}$ as a function of roughness H_{rms}. Symbols differentiate measurement type and color indicates hotspots as in Figures 4b and 4c. Vertical profiles of (b) ϵ and (c) K_ρ referenced to height above bottom are shown for the mean of all stations (gray), and separately for the mean of non-hotspot stations (blue), the 2200-m hotspot (red) and the 1300-m hotspot (green). Data in Figures 4b and 4c are simple averages of occupation means (i.e., all labeled profiles in Figure 2 are weighted equally). For hotspots, shading represents the full span of occupation-mean data; for non-hotspots it represents the range spanned by the upper 2/3 of data. The non-hotspot mean (blue) has similar structure and magnitude to that observed over other rough bathymetry as approximately represented by the dashed curve (consistent with vertical profiles over the Mid-Atlantic Ridge [*Ledwell et al.*, 2000], Oregon slope [*Moum et al.*, 2002], Virginia slope [*Nash et al.*, 2004] and Hawaiian Ridge [*Klymak et al.*, 2006].)

10^{-8} W/kg – large and similar to that measured by *Moum et al.* [2002] over the 1600–2000-m isobaths. At the hotspots, the dissipation rate is 7–14 times larger ($\langle\epsilon\rangle_{500}^{2200-hotspot}$ = 9.0 × 10^{-8} W/kg and $\langle\epsilon\rangle_{500}^{1300-hotspot}$ = 4.7 × 10^{-8} W/kg, vertically integrating to 24–45 mW/m^2). Including the hotspots, the slope average dissipation (weighted by the spacing of our sampling) is $\langle\epsilon\rangle_{500}^{slope}$ = 3.2 × 10^{-8} W/kg (15 mW/m^2 integrated). Hence, the hotspots contribute to about 80% of the slope-integrated turbulent dissipation of 0.5 kW per meter coastline.

[18] Assuming a mixing efficiency of 0.2, 0.6 kW/m of energy must be supplied to effect the combined energy dissipation and buoyancy flux. In the following, we compare this requirement to the energy available from local and remote sources.

4.1. Local Sources

[19] Assimilation of altimetric data into barotropic tidal models permits tidal energy dissipation to be estimated [*Egbert and Ray*, 2001]. These losses feed both internal tide generation/radiation and local turbulent energy dissipation. Analysis of TPXO.5 barotropic losses (updated model solutions courtesy Gary Egbert) indicate a band of elevated tidal dissipation with mean of 5.8 mW/m^2 in an 80-km-wide region centered over the Oregon slope from 42–46°N. This equates to a mean barotropic loss over the slope of 0.46 kW/m, slightly less than the 0.6 kW/m computed above. Since generation of low-mode waves (which can propagate and hence dissipate far away) is weak here [*Niwa and Hibiya*, 2001; *Simmons et al.*, 2004a], the bulk of the 0.46 kW/m is presumably due to high-mode waves that dissipate locally. Consistent with this interpretation, the spectral level of generated waves computed following *St. Laurent and Garrett* [2002] (i.e., assuming linear generation and subcritical bathymetry – an assumption violated here) is a factor of two higher on the Oregon slope compared to the Mid-Atlantic Ridge. Local generation is effected primarily by topographic scales not resolved by global satellite data sets and appears to account for the observed dissipation.

4.2. Remote Sources

[20] Baroclinic energy fluxes computed at the offshore mooring (M1, 100 km from the slope) following *Kunze et al.* [2002], *Alford* [2003] and *Nash et al.* [2005], were (1) temporally variable on 4–10 day time-scales, (2) predominantly mode 1, and (3) onshore at O(1 kW/m) during our shipboard observations. Hence, dissipation of these incident waves in the bottom 500 m through interaction with rough [*Thorpe*, 1992] or near-critical bathymetry [*Eriksen*, 1998; *Nash et al.*, 2004] could also account for the observed dissipation. Since a remotely-generated internal tide is likely to have wandering phase [*Rainville and Pinkel*, 2005], the apparent barotropic phasing of turbulence at station 2.5 (over the five-day timescale between occupations) favors local generation at that site. However, remote sources may be important elsewhere on the slope (at station 4.3, for example). This is a subject of current investigation.

5. Conclusions

[21] Intense turbulence ($\epsilon \sim 10^{-8} - 10^{-7}$ W/kg, $K_\rho \sim 10^{-4} - 10^{-2}$ m^2/s) within 500 mab was observed over a 20-km cross-slope section of the Oregon slope with enhanced 200–1000-m horizontal-scale roughness. From energetics, the turbulence may be driven by breaking of either local tidally-generated internal waves or a remotely-generated low-mode tide. At the hotspots, turbulence is ten times that observed elsewhere on the slope, driving time-average $K_\rho \sim 10^{-2}$m^2/s that are comparable to those observed in deep overflows [*Ferron et al.*, 1998; *Thurnherr et al.*, 2002]. While turbulence appears phase-locked to the semidiurnal tide at both hotspots, differences in vertical structure and phasing at each site suggest that the turbulence generation mechanisms may be different.

[22] The bottom roughness of our cross-section (Figure 2a) is not statistically different from the rest of the Oregon continental slope: in both our cross-section and in the domain shown in Figure 1b, 12% of the bottom has H_{rms} > 20 m. We thus argue that our cross-slope section is typical of the Oregon slope, so that (1) similar flows and turbulence are to be expected elsewhere on the slope and

(2) our energetics calculations are representative of the broader continental slope.

[23] As inferred from satellite altimetry [*Egbert and Ray*, 2001], this region is one of modest barotropic tidal dissipation compared to major deep-water sites like the Hawaiian Ridge [*Rudnick et al.*, 2003] and Aleutian Islands [*Cummins et al.*, 2001], where generated internal tides are low-mode [*Simmons et al.*, 2004a; *Niwa and Hibiya*, 2001] and radiate thousands of kilometers. Wide continental shelves with significant cross-shelf tidal flow like the Bay of Biscay [*Pingree and New*, 1989] and the northern Australian coast [*Holloway et al.*, 2001] are also strong generators of low-mode radiating waves. In contrast, tidal currents over the Oregon slope generally parallel the large-scale isobaths, so that the barotropic loss can be entirely accounted for by local turbulent dissipation. However, remote sources such as deep-ocean internal waves impinging on the slope may also contribute to the observed turbulent dissipation.

[24] Our observations suggest that topographic roughness at scales not resolved in global bathymetric datasets is a controlling factor for generating turbulent mixing over the Oregon slope. Because (1) tidal currents tend to be stronger on continental slopes than in the deep ocean [*Egbert*, 1997] and (2) continental slopes have similar small-scale roughness as the major geological spreading centers, continental slopes may play an important role in global mixing and energy budgets. We hypothesize that topography unresolved by global satellite data sets (i.e., 200-2000 m scales) at these and other locations is responsible for a significant fraction of the deep-ocean mixing.

[25] Wave generation at such sites is at wavenumbers too high to be captured in models run with low-resolution bathymetry [*Simmons et al.*, 2004a; *Niwa and Hibiya*, 2001]. However, *St. Laurent et al.* [2002] have proposed a mixing parameterization scheme based on topographic roughness and barotropic tide ellipses which has been implemented in global models by *Simmons et al.* [2004b], *Saenko and Merryfield* [2005] and others. If high-resolution global bathymetry datasets become available, similar schemes (including both roughness-based closures and a crude representation of the low-mode internal tide) may be a means to predict the global distribution of deep mixing.

[26] **Acknowledgments.** We thank Dicky Allison, Eric Boget, Andrew Cookson, Richard Dewey, Eleanor Frajka Williams, Ray Kreth, Dave Winkel, Zhongxiang Zhao, and the captain and crew of the Wecoma for their technical expertise and at-sea contributions; Mark Merrifield and Nathalie Zilberman for their generosity in performing model runs to help site our study; Murray Levine, Knut Aagard, Rebecca Woodgate, and Charlie Eriksen for loaning mooring instruments; Martin Visbeck and Andreas Thurnherr for LADCP software and advice; Gary Egbert for TOPEX/POSEIDON dissipation estimates; Lou St. Laurent for linear wave generation code; and two anonymous reviewers for their constructive comments. This project was supported by NSF grants OCE-0350543 and OCE-0350647.

References

Alford, M. H. (2003), Energy available for ocean mixing redistributed by long-range propagation of internal waves, *Nature*, *423*, 159–162.

Alford, M. H., and R. Pinkel (2000), Observations of overturning in the thermocline: The context of ocean mixing, *J. Phys. Oceanogr.*, *30*(5), 805–832.

Alford, M. H., M. C. Gregg, and M. A. Merrifield (2006), Structure, propagation and mixing of energetic baroclinic tides in Mamala Bay, Oahu, Hawaii, *J. Phys. Oceanogr.*, *36*(6), 997–1018.

Baines, P. G. (1982), On internal tide generation models, *Deep Sea Res., Part A*, *29*(3), 307–338.

Cummins, P. F., J. Y. Cherniawski, and M. G. Foreman (2001), North Pacific internal tides from the Aleutian Ridge: Altimeter observations and modelling, *J. Mar. Res.*, *59*, 167–191.

Dillon, T. M. (1982), Vertical overturns: A comparison of Thorpe and Ozmidov length scales, *J. Geophys. Res.*, *87*, 9601–9613.

Egbert, G. D. (1997), Tidal data inversion: Interpolation and inference, *Prog. Oceanogr.*, *40*, 81–108.

Egbert, G. D., and R. D. Ray (2001), Estimates of M2 tidal energy dissipation from TOPEX/POSEIDON altimeter data, *J. Geophys. Res.*, *106*, 22,475–22,502.

Eriksen, C. C. (1998), Internal wave reflection and mixing at Fieberling Guyot, *J. Geophys. Res.*, *103*, 2977–2994.

Ferron, B., H. Mercier, K. Speer, A. Gargett, and K. Polzin (1998), Mixing in the Romanche Fracture Zone, *J. Phys. Oceanogr.*, *28*(10), 1929–1945.

Garrett, C., and E. Kunze (2007), Internal tide generation in the deep ocean, *Annu. Rev. Fluid Mech.*, *39*, 57–87.

Goff, J. A., and T. H. Jordan (1988), Stochastic modeling of seafloor morphology: Inversion of sea beam data for second-order statistics, *J. Geophys. Res.*, *93*, 13,589–13,608.

Gregg, M. C. (1989), Scaling turbulent dissipation in the thermocline, *J. Geophys. Res.*, *94*, 9686–9698.

Gregg, M. C., and E. Kunze (1991), Shear and strain in Santa Monica Basin, *J. Geophys. Res.*, *96*, 16,709–16,719.

Holloway, P. E., P. G. Chatwin, and P. Craig (2001), Internal tide observations from the Australian North West Shelf in summer 1995, *J. Phys. Oceanogr.*, *31*(5), 1182–1199.

Klymak, J. M., J. N. Moum, J. D. Nash, E. Kunze, J. B. Girton, G. S. Carter, C. M. Lee, T. B. Sanford, and M. C. Gregg (2006), An estimate of energy lost to turbulence at the Hawaiian Ridge, *J. Phys. Oceanogr.*, *36*(6), 1148–1164.

Kunze, E., and S. G. Llewellyn Smith (2004), The role of smallscale topography in turbulent mixing of the global ocean, *Oceanography*, *17*(1), 55–64.

Kunze, E., L. K. Rosenfeld, G. S. Carter, and M. C. Gregg (2002), Internal waves in Monterey Submarine Canyon, *J. Phys. Oceanogr.*, *32*(6), 1890–1913.

Ledwell, J., E. Montgomery, K. Polzin, L. St. Laurent, R. Schmitt, and J. Toole (2000), Evidence for enhanced mixing over rough topography in the abyssal ocean, *Nature*, *403*, 179–182.

Legg, S. (2004), Internal tides generated on a corrugated continental slope: part 2: Along-slope barotropic forcing, *J. Phys. Oceanogr.*, *34*(8), 1824–1838.

Levine, M. D., and T. J. Boyd (2006), Tidally forced internal waves and overturns observed on a slope: Results from the HOME, *J. Phys. Oceanogr.*, *36*(6), 1184–1201.

Moum, J. N., D. Caldwell, J. D. Nash, and G. Gunderson (2002), Observations of boundary mixing over the continental slope, *J. Phys. Oceanogr.*, *32*(7), 2113–2130.

Nash, J. D., E. Kunze, J. M. Toole, and R. W. Schmitt (2004), Internal tide reflection and turbulent mixing on the continental slope, *J. Phys. Oceanogr.*, *34*(5), 1117–1134.

Nash, J. D., M. H. Alford, and E. Kunze (2005), Estimating internal wave energy fluxes in the ocean, *J. Atmos. Oceanic Technol.*, *22*(10), 1551–1570.

Niwa, Y., and T. Hibiya (2001), Numerical study of the spatial distribution of the M_2 internal tide in the Pacific Ocean, *J. Geophys. Res.*, *106*, 22,441–22,449.

Osborn, T. R. (1980), Estimates of the local rate of vertical diffusion from dissipation measurements, *J. Phys. Oceanogr.*, *10*(1), 83–89.

Pingree, R. D., and A. L. New (1989), Downward propagation of internal tidal energy into the Bay of Biscay, *Deep Sea Res.*, *36*, 735–758.

Polzin, K. L. (2004), Idealized solutions for the energy balance of the finescale internal wavefield, *J. Phys. Oceanogr.*, *34*(1), 231–246.

Rainville, L., and R. Pinkel (2005), Propagation of low-mode internal waves through the ocean, *J. Phys. Oceanogr.*, *36*(6), 1220–1236.

Romsos, C. G., C. Goldfinger, R. Robison, R. L. Milstein, J. D. Chaytor, and W. W. Wakefield (2006), Development of a regional seafloor surficial geologic habitat map for the continental margins of Oregon and Washington, USA, in *Marine Geological and Benthic Habitat Mapping*, *Geol. Assoc. Can. Spec. Publ.*, edited by H. G. Greene and B. J. Todd, Geol. Assoc. of Can., St. John's, Newfoundland, in press.

Rudnick, D. L., et al. (2003), From tides to mixing along the Hawaiian Ridge, *Science*, *301*(5631), 355–357.

Saenko, O. A., and W. J. Merryfield (2005), On the effect of topographically enhanced mixing on the global ocean circulation, *J. Phys. Oceanogr.*, *35*(5), 826–834.

Simmons, H., R. Hallberg, and B. Arbic (2004a), Internal wave generation in a global baroclinic tide model, *Deep Sea Res., Part II*, *51*, 3043–3068.

Simmons, H. L., S. R. Jayne, L. C. St. Laurent, and A. J. Weaver (2004b), Tidally driven mixing in a numerical model of the ocean general circulation, *Ocean Modell.*, *6*, 245–263, doi:10.1016/S1463-5003(03)00011-8.

St. Laurent, L., and C. Garrett (2002), The role of internal tides in mixing the deep ocean, *J. Phys. Oceanogr.*, *32*(10), 2882–2899.

St. Laurent, L., and J. D. Nash (2004), An examination of the radiative and dissipative properties of deep ocean internal tides, *Deep Sea Res., Part II*, *51*, 2042–3029.

St. Laurent, L., H. L. Simmons, and S. R. Jayne (2002), Estimating tidally driven mixing in the deep ocean, *Geophys. Res. Lett.*, *29*(23), 2106, doi:10.1029/2002GL015633.

Thorpe, S. A. (1992), The generation of internal waves by flow over the rough topography of a continental slope, *Proc. R. Soc. London, Ser. A*, *439*, 115–130.

Thurnherr, A. M., K. J. Richards, C. R. German, G. F. Lane-Serff, and K. G. Speer (2002), Flow and mixing in the rift valley of the Mid-Atlantic Ridge, *J. Phys. Oceanogr.*, *32*(6), 1763–1778.

M. H. Alford and K. Martini, Applied Physics Laboratory, University of Washington, 1013 NE 40th Street, Seattle, WA 98105, USA.

S. Kelly and J. D. Nash, College of Oceanic and Atmospheric Sciences, Oregon State University, 104 COAS Admin Building, Corvallis, OR 97331, USA. (nash@coas.oregonstate.edu)

E. Kunze, School of Earth and Ocean Science, University of Victoria, P.O. Box 3055 STN CSCC, Victoria, BC, Canada V8W 3P6.